Darrieus wind turbine blade unsteady aerodynamics: a three-dimensional Navier-Stokes CFD assessment

Publisher's version at DOI:10.1016/j.energy.2017.04.017

Darrieus Wind Turbine Blade Unsteady Aerodynamics: a Three-Dimensional Navier-Stokes CFD assessment

Francesco Balduzzi[1], Jernej Drofelnik[2], Alessandro Bianchini[1], Giovanni Ferrara[1], Lorenzo Ferrari[3*], Michele Sergio Campobasso[4]

[1] Department of Industrial Engineering, University of Florence - Via di Santa Marta 3, 50139, Firenze, Italy - Tel. +39 055 275 8773 - Fax +39 055 275 8755 - balduzzi@vega.de.unifi.it

[2] School of Engineering, University of Glasgow - James Watt Building South, University Avenue, G12 8QQ Glasgow, UK - Tel. +44 (0)141 330 2032 - j.drofelnik.1@research.gla.ac.uk

[3] CNR-ICCOM, National Research Council of Italy - Via Madonna del Piano 10, 50019 Sesto Fiorentino, Italy - Tel. +39 055 5225 218 - Fax +39 055 5225 203 - lorenzo.ferrari@iccom.cnr.it

[4] Department of Engineering, Lancaster University - Gillow Avenue - LA1 4YW Lancaster, UK - Tel. +44 (0)1524 594673 - Fax +44 (0)1524 381707 - m.s.campobasso@lancaster.ac.uk

[*] = contact author

Abstract

Thanks to the recent rapid progress in high-performance computing and the growing availability of large computational resources, computational fluid dynamics now offers a cost-effective, versatile and accurate means to improve the understanding of the unsteady aerodynamics of Darrieus wind turbines, increase their efficiency and delivering more cost-effective structurally sound designs.

In this study, a Navier-Stokes CFD research code featuring a very high parallel efficiency was used to thoroughly investigate the three-dimensional unsteady aerodynamics of a one-blade Darrieus rotor. Highly spatially and temporally refined time-dependent simulations were carried out using up to 16,000 processor cores per simulation on an IBM BG/Q cluster. The study aims at providing a detailed description and quantification of the main three-dimensional effects associated with the cyclical motion of this turbine type, including tip losses, dynamic stall, vortex propagation and blade/wake interaction. On one hand, the results corroborate the findings of several carefully designed two-dimensional studies. On the other hand, they reveal that the three-dimensional flow effects affecting Darrieus rotor blades are much more complex than assumed by the conventional lower-fidelity models often used for design applications, and strongly vary during the rotor revolution.

Keywords

Darrieus wind turbine, unsteady Navier-Stokes simulations, CFD, tip-effects, 3D flows

Nomenclature

<u>*Latin symbols*</u>

AoA angle of attack

AR	aspect ratio	[-]
c	blade chord	[m]
C_m	moment coefficient	[-]
C_p	pressure coefficient on airfoils	[-]
BEM	Blade Element Momentum	
CFD	Computational Fluid Dynamics	
H	turbine height	[m]
k	turbulent kinetic energy	[m^2/s^2]
NS	Navier-Stokes	
p	static pressure	[Pa]
R	turbine radius	[m]
T	torque per unit length	[Nm]
TKE	turbulent kinetic energy	
TSR	tip-speed ratio	[-]
U	wind speed	[m/s]
U_z	vertical velocity component	
VAWTs	Vertical-Axis Wind Turbines	
w_{th}	theoretic relative wind speed	[m/s]
x, y, z	reference axes	
y^+	dimensionless wall distance	[-]

Greek symbols

ϑ	azimuthal angle	[deg]
μ_t	turbulent viscosity	[Kg/m/s]
ρ	air density	[kg/Nm^3]
Φ	computational domain diameter	[m]
Ψ	computational domain height	[m]
ω	specific turbulence dissipation rate	[1/s]
Ω	turbine revolution speed	[rad/s]

Subscripts

∞	value at infinity
ave	averaged value

1. Introduction

1.1 Background

After most research projects on vertical-axis wind turbines (VAWTs) came to a standstill in the mid 90's [1], the Darrieus wind turbine [2] is receiving rapidly increasing attention of both researchers and manufacturers [3-5]. For distributed wind power generation in the built environment [6], inherent advantages of this turbine type, such as performance independence on wind direction, generator often positioned on the ground, low noise emissions [7], enhanced performance in skewed flows [8] may outweigh disadvantages such as lower power coefficients and more difficult start-up with respect to typical horizontal axis machines. Moreover, in densely populated areas VAWTs are often preferred to other turbine types because they are perceived as aesthetically more pleasant and thus easier to integrate in the landscape [9]. The applicability of Darrieus wind turbine for utility-scale power generation making use of floating platforms also appears to present important benefits in terms of overall dynamic stability [10].

Historically, the aerodynamic performance analysis of these rotors has been carried out with low-fidelity methods, like the Blade Element Momentum (BEM) theory [1,11-13] or lifting line methods [14-15]. More recently, however, the intrinsic limitations of these models made clear that higher-fidelity tools are needed in order to understand in greater depth the complex physical phenomena taking place during the revolution of Darrieus rotors [16], like the interaction of the blades with macro vortices [17] or dynamic stall [18].

If experimental testing is often extremely difficult and expensive, Navier-Stokes (NS) Computational Fluid Dynamics (CFD) can provide versatile and accurate means to improve the understanding of VAWT unsteady aerodynamics and achieve higher-performance, structurally sound and more cost-effective Darrius turbine designs. The use of NS CFD for simulating time-dependent Darrieus turbine aerodynamics is rapidly increasing due to both the ongoing development and deployment of more powerful high-performance computing hardware, such as large clusters of multi- and many-core processors [19], and also the development of computationally more efficient algorithms.

1.2 Previous CFD studies on Darrieus VAWTs

Early assessments of the Reynolds-Averaged Navier-Stokes (RANS) CFD technology for Darrieus rotor aerodynamics, aiming primarily at thoroughly investigating the complex fluid mechanics of these machines, made use mainly of a two-dimensional (2D) approach (e.g. [20-21]); an extensive literature review on these studies has been recently provided by Balduzzi et al. [22]. The use of a 2D approach was motivated by the need of maintaining the computational cost of the simulations within acceptable limits, since the fully-unsteady solution of the three-dimensional (3D) flow field past rotating Darrieus rotors requires very large computational resources due to the very large temporal and spatial grid refinement needed for obtaining reliable results [22-24]. Unfortunately, the use of 2D simulations results in some important aerodynamic features being discarded (e.g. tip flow effects, secondary flows, etc.). Notwithstanding this, recent work [25-28] showed that properly-set 2D approach can provide estimations of the power curve of a rotor relatively close to the experimental value and, thus, usable for preliminary design.

Since the early 2D studies of Darrieus rotor aerodynamics based 2D NS CFD, researchers have longed to perform 3D simulations of these machines in order to fully understand some phenomena that are presently modeled on the basis of a relatively small amount of data from existing turbines and assumptions based on overly simplistic analytical models.

In the past few years, thanks to the growth of available computational resources, 3D NS CFD analyses have received increasing attention, and some preliminary studies have been published. First, comparisons between two-dimensional simulations and three-dimensional ones have been carried out (e.g. [29]). Purely 3D studies have been also carried out to characterize the turbine wake [29], the flow field around the blades [30-31], the start-up of small rotors [32], the effects of the finite aspect ratio [33-34] or the influence of supporting arms [35] and different blade shapes [36]. Finally, further studies were also focused on the performance variation in skewed flow conditions [37-38].

Although many of the aforementioned analyses have indeed highlighted new important aerodynamic phenomena, in almost all cases limited computational resources imposed the use of fairly coarse spatial and temporal refinements, which often did not match the requirements indicated by proper sensitivity analyses. In particular, the common approach found in the literature was to progressively coarsen the meshes when moving to 3D analyses, in order to limit the total number of cells in the range between 1,000,000 and 10,000,000.

Most recent 2D parametric CFD analyses of Darrieus rotors (e.g. [22-24]) showed that the simulation reliability is tremendously affected by the quality of the meshing and time-stepping strategies. In particular, it has been shown that the minimum temporal and spatial refinement levels required to obtain grid-independent solutions is quite high, due to the aerodynamic complexity of these unsteady rotor flows. Therefore, when using 3D unsteady NS CFD for Darrieus rotor aerodynamics, the computational cost of the simulation becomes very large due to necessity of maintaining high levels of time-refinement and a high level of spatial refinement both in the grid planes normal to the rotor axis and the axialwise direction. Refinement in the latter direction is mandatory to reliably resolve 3D flow features. Failing to maintain suitably high grid refinement levels in all three direction results in losing the potential of 3D simulations of improving the design of these machines by properly resolving 3D effects. As an example, one of the previous studies based on 2D RANS CFD showed that temporal and spatial grid-independent solutions are obtained provided that grids with at least 400,000 elements are used [22]. To preserve the same accuracy level in a 3D RANS simulation of the same turbine (modelling only half of the rotor making use of symmetry boundary conditions on the plane at rotor midspan) the mesh would consist of about 90,000,000 cells, which is almost ten times the size of the finest meshes used in the 3D RANS studies of Darrieus rotor flows published to date.

1.3 Study aim

In this study, a RANS CFD research code featuring a very high parallel efficiency is used to investigate the detailed features of 3D flow effects of a rotating Darrieus rotor blade and the impact of such effects on the power generation efficiency of the blade. To accomplish this, a time-dependent 3D simulation using very high levels of spatial and temporal refinements and yielding a fairly reliable assessment of the phenomena under investigation is carried out using a large 98,304-core IBM BG/Q cluster. The scope of the study is to analyze the main 3D effects occurring during the cyclic motion of the considered one-blade rotor configuration, including tip vortices, dynamic stall and downstream vortex propagation, and to assess the impact of these phenomena on the overall performance of this rotor.

The paper is organized as follows: sections 2 and 3 summarize the main features of the case study and the numerical framework, respectively. Section 4 presents the main results of the 3D analysis and compares them to those of the 2D analysis of the same case study, in order to highlight the impact of 3D effects by comparing the integral performance of a finite-length rotor and that of the infinite blade counterpart. A summary of the study and concluding remarks are finally provided in section 5.

2. Case study

The case study selected for the 3D simulation is a one-blade H-Darrieus rotor using a NACA 0021 airfoil. The chord (c=0.0858 m) and radius (R=0.515 m) of this virtual rotor were taken equal to those used in the case-study of [21]; the blade was attached at midchord. In order to reduce the computational cost of the simulation, the central symmetry of H-Darrieus rotors was exploited, allowing to simulate only one half of the blade rather than the entire blade length of H=1.5 m. Thus, the aspect ratio (AR) of the simulated blade portion is 8.74 which is half that of the actual blade. The blade was contained in a cylindrical computational domain (Fig. 1) having a radius Φ=240R, a value chosen to guarantee a full development of the wake [26]. The domain height was instead set to Ψ=2.53H, corresponding to half the height (due to the central blade symmetry) of the wind tunnel where the original model was tested [21,39]; data of these tests were used for the validation of the numerical RANS CFD approach [26-28], that can be viewed as the 2D counterpart of the 3D methodology used in the present study.

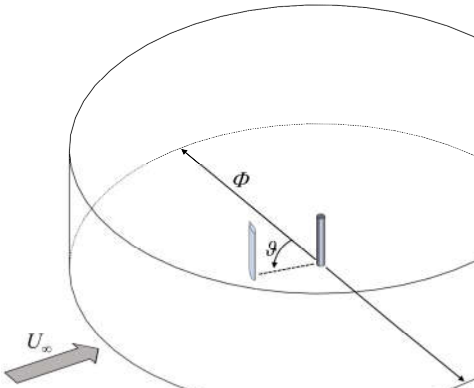

Figure 1 - Computational domain.

The 3D mesh (details are reported in Fig. 2) was obtained by first generating a 2D mesh past the airfoil using the optimal mesh settings identified in [26-27], and then extruding this mesh in the spanwise (z) direction and filling up with grid cells the volume between the blade tip and the circular farfield boundary.

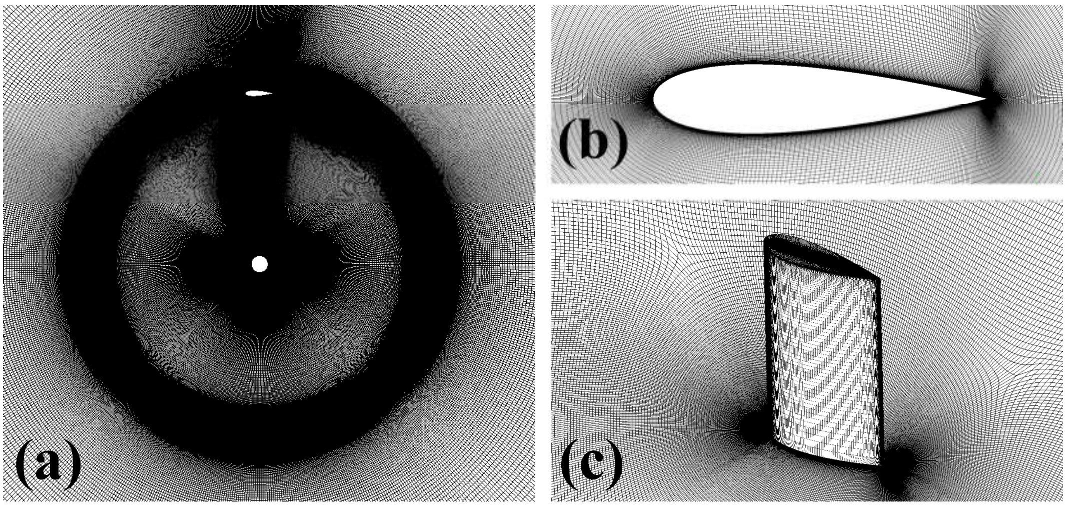

Figure 2 - Some details of the computational mesh.

The 3D grid is structured multi-block. Its 2D section normal to the z-axis and in the z-interval occupied by the blade (Fig. 2(a)) consisted of 4.3×10^5 quadrilateral cells. The airfoil was discretized with 580 nodes and the first element height was set to $5.8 \times 10^{-5}c$ to guarantee a dimensionless wall distance y^+ lower than 1 throughout the revolution. As recommended in [22], a proper refinement of both leading and the trailing edge regions was adopted (Fig. 2(b)), as well as a globally high refinement in the region around the airfoil within one chord from the walls in order to properly resolve the detached flow regions at high angle of attack (AoA) [40]. After extrusion in the z direction, 80 layers in the half-blade span were formed (Fig. 2(c)), with progressive grid clustering from midspan to the tip in order to ensure an accurate description of tip flows. Moreover, a high grid refinement level was provided in the whole tip region above the blade in order to properly capture the flow separation and the tip vortices. The final mesh was made of 64×10^6 hexahedral cells and able to fulfill the numerical requirements prescribed in [24].

Due to the large burden associated with running the 3D time-dependent simulation, only a single operating condition was simulated, corresponding to a tip-speed ration (*TSR)* of 3.3. The free stream wind speed was U=9 m/s. The turbulence farfield boundary conditions were a turbulent kinetic energy (k) based on 5% turbulence intensity and a characteristic length of 0.07 m (according to [27], production limiters were used in the simulations on k and ω with a setting ratio of 10).

3. Computational framework

All RANS simulations were carried out with the COSA research code.

COSA is a compressible density-based structured multi-block finite volume RANS code featuring a steady flow solver, a time-domain (TD) solver for the solution of general unsteady problems [41-42], and a harmonic balance solver for the rapid solution of periodic flows [43-45]. The RANS equations are obtained by time-averaging the Navier-Stokes equations on the characteristic turbulent time-scales of the problem at hand. The RANS equations are formally similar to the Navier-Stokes equations, and differ from those for the fact that all thermodynamic and kinematic variables are mean rather than instantaneous values, and for the presence of an additional term, the Reynolds stress tensor accounting in a mean fashion for the effects of turbulence. Making use of Boussinesq's approximation, the Reynolds stress tensor is given by the product of an eddy viscosity μ_t and the strain rate tensor of the mean velocity field. COSA determines μ_t with Menter's k-ω shear stress transport turbulence model [46]. The second-order space discretization of the convective fluxes of both the RANS and the SST equations uses an upwind scheme based on Van Leer's MUSCL extrapolations and Roe's flux difference splitting. The second order discretization of all diffusive fluxes is instead based on central finite-differencing. The space-discretized RANS and SST equations are integrated in a fully-coupled fashion with an explicit solution strategy based on full approximation scheme multigrid featuring a four stage Runge-Kutta smoother. Convergence acceleration is achieved by means of local time-stepping and implicit residual smoothing. For general time-dependent problems, the TD equations are integrated using a second order dual time-stepping approach.

Comprehensive validation analyses of COSA are reported in [43,45] and other references cited therein. For unsteady problems involving oscillating wings and cross-flow open rotors such as the Darrieus rotor configuration investigated in this paper, COSA solves the governing equations in the absolute frame of reference using an arbitrary Lagrangian-Eulerian formulation and body-fitted grids. In the case of Darrieus rotors this implies that the entire computational grid rotates about the rotational axis of the turbine. The suitability of COSA for the simulation of Darrieus wind turbines has been recently assessed through comparative analyses with both commercial research codes and experimental data [26-27].

Present simulations were run on an IBM BG/Q cluster [47], featuring 8,144 16-core nodes with a total of 98,304 cores. Thanks to the excellent parallel efficiency of the COSA code, the simulations yielding the results presented in this paper could be performed using about 16,000 cores. This required partitioning the grid into 16384 blocks, making use of in-house utilities. Using a time-discretization of 720 steps per revolution, the simulation needed 12 revolutions to achieve a fully periodic state. The flow field over the consider period was assumed to be periodic once the difference between the mean torque of the last two revolutions was smaller than 0.1% of the mean torque in the revolution before the last. The wall-clock time required for the complete simulation was about 653 hours (27.2 days).

4. Results

Figure 3(a) reports the periodic profile of the torque coefficient per unit blade length at different span lengths along the blade (0% and 100% correspond to midspan and tip, respectively). The angular position ϑ=0° corresponds to the blade leading edge facing the oncoming wind and entering the upwind half of its revolution.

The instantaneous torque coefficient per unit length C_{mz} is defined by Eq. (1). Here T_z denotes the instantaneous torque per unit blade length at the considered z position, U_∞ and ρ_∞ denote the wind speed and the air density, respectively, and c denotes the blade chord.

$$C_{mz} = \frac{T_z}{\frac{1}{2}\rho_\infty U_\infty^{\ 2} c^2} \tag{1}$$

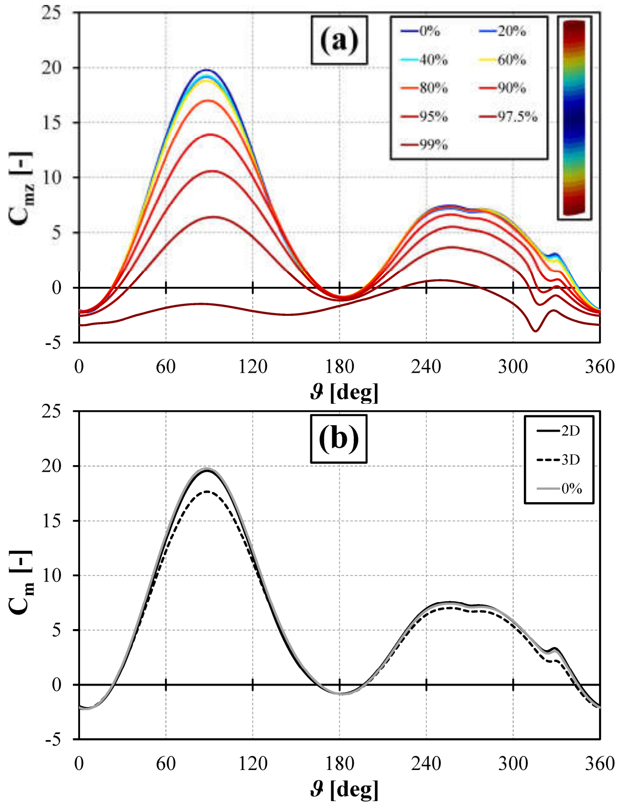

Figure 3 - Moment coefficient vs azimuthal angle: (a) variation at different span lengths; (b) 2D simulations compared to the 3D profile at midspan and average 3D profile.

Figure 3(b) reports three torque profiles. One, that labelled *2D*, refers to the results of a 2D simulation of the same rotor, and corresponds to the "ideal" torque of a blade with infinite span, i.e. without any secondary effects at the blade tip. This 2D simulation was carried out using a mesh equal to the midspan section of the 3D mesh and the same numerical parameters of the 3D simulations. The torque profile labelled *0%* is the torque per unit blade length at the midspan position of the finite-length rotor, whereas the torque profile labelled *3D* is the overall torque coefficient C_m of the 3D rotor defined as:

$$C_m = \frac{2}{H}\int_0^{\frac{H}{2}} C_{mz}\, dz \tag{2}$$

Examination of these profiles reveals several important facts. Firstly, the ideal 2D torque and the 3D torque profiles are characterized by similar patterns, including the occurrence of two relative maxima, one in the upwind the other in the downwind regions, and also similar blade azimuthal positions of both maxima: the maximum torque in the upwind portion of the revolution is located at ϑ≈88.5° and the maximum torque in the downwind portion of the revolution is located at $\vartheta\approx257°$ in both cases. An almost perfect match is visible between the 2D curve and the curve at midspan of the 3D rotor, highlighting that 3D flow effects due to tip flows do not reach this position.

Examination of all profiles of Fig. 3(b) shows that the effects of blade finite-length effects are very small when the blade loading is low, i.e. when the angle of attack on the airfoil is low (azimuthal positions between $0°<\vartheta<40°$, $130°<\vartheta<210°$): in these portions of the revolution, the 2D and both 3D curves (i.e. the local profile at 0% span and the average one) are indeed almost superimposed. When the incidence increases, the blade load also increases. Consequently, torque reduction due to tip effects also increases both in the upwind and the downwind zones. This is because the strength of tip vortex flow increases with the flow incidence. By further looking at the comparison between the 2D curve and the mean 3D curve, one can notice that these effects are strongest in the upwind region of the period, where a maximum difference of 9.7% between the torque peaks occurs.

Focusing now on the torque profiles at different semispan lengths reported in Fig. 3(a), some additional observations can be made, more specifically:

- The torque profiles of the blade sections at 20%, 40% and 50% of the semispan are almost identical, indicating that at least half of the blade is characterized by a predominantly 2D flow with negligible impact of tip flow effects;
- The torque profiles of the blade sections at 60%, 70% and 80% start showing a progressive reduction of the torque peak, down to -14% with respect to the midspan section. The remainder of the torque curve is less affected, especially in the downwind zone;
- The torque profiles of the blade sections at 90%, 95% and 97.5% show that at these distances from the blade tip the 3D effects are strong throughout the whole revolution. In particular, in the regions of positive torque production, the efficiency is remarkably reduced;
- In proximity of the blade tip (99%) almost no positive contribution to the torque output is given, due to the large load reduction;
- In general, the azimuthal position of the torque peak occurs later in the cycle as one moves towards the tip, with a 5° shift between the 0% and 97.5% sections. This can be explained with a reduction of the incidence angle (downwash), as will be shown in continuation of the study.

To quantify the predicted impact of tip effects in comparison to existing knowledge, Fig. 4 reports the comparison of the 2D and mean 3D torque profiles obtained with the CFD analyses and the corresponding estimates obtained with the VARDAR research code, a state-of-the-art BEM code developed at the University of Florence [6,13-14] using the ubiquitous Leicester-Prandtl model for the finite-wing correction [48].

The two BEM profiles of Fig. 4 differ in that one includes tip flow corrections and the other does not.

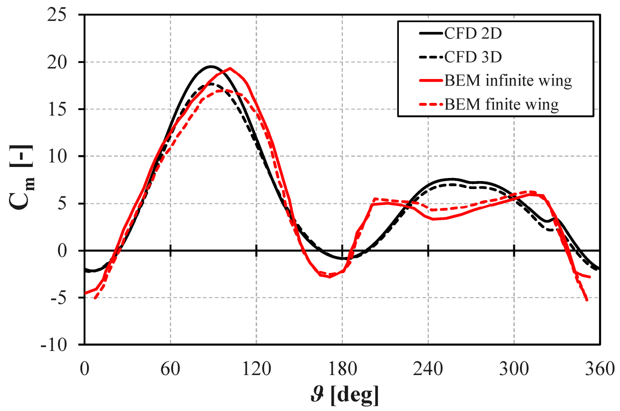

Figure 4 - Moment coefficient profiles: 2D and 3D CFD data vs. BEM simulations either including or neglecting the finite-wind effects.

Examination of these profiles highlights, that the extent of the upwind moment peak reduction predicted by the CFD analyses is in good agreement with that estimated with the simplified tip flow model included in the BEM theory. On the other hand, the lumped parameter model appears not to be able to properly capture the moment coefficient reduction in the downwind portion of the revolution. Conversely to the CFD results, the BEM model in fact predicts a slight moment increase downwind, since the lower energy extraction predicted in the upwind zone leads to a lower induction factor and then to a higher attended wind speed in the downwind flow. This comparative analysis highlights the potential of using CFD for further improving the analysis, and ultimately the design, of Darrieus rotor aerodynamics since it may provide a new insight for the calibration of proper corrections in lower-order models.

To provide a different quantitative perspective of the impact of tip losses, Fig. 5 reports the profile of mean moment coefficient per unit length. The mean value for each blade height is obtained by averaging the profiles of Fig. 3(a) over one revolution. The figure also reports the constant mean torque values of the 2D and 3D simulations for both the CFD and BEM models. All curves are normalized with respect to the mean 2D moment coefficient.

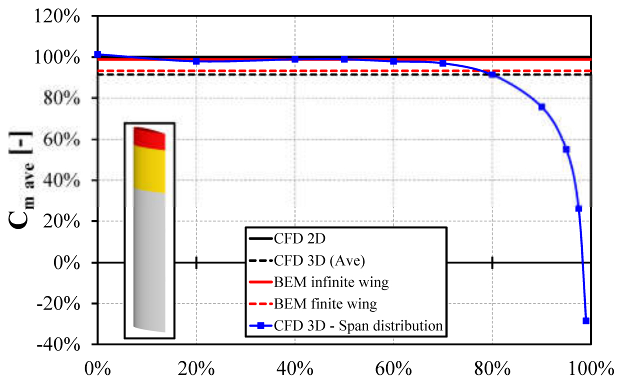

Figure 5 - Moment coefficient distribution along the semispan.

One sees that the average blade performance is almost unaffected by tip-effects up to approximately 70% of its semispan. Expressing these results with reference to the blade chord and aspect ratio, it is found that tip flow effects adversely affect the performance of the blade for a span length of approximately 2.6*c* (yellow zone in Fig. 5). In terms of aggregate data, the tip effects yield a reduction of the rotor torque of 8.6% with respect to the theoretical 2D calculation with virtually infinite span. This can be globally seen as an equivalent reduction of the actual blade's height by 0.75*c* (red colored zone in Fig. 5) and such a correction factor needs to be accounted for when estimating the turbine's performance by means of 2D CFD simulations.

To further investigate the phenomena that lead to the efficiency reduction, the Mach contours and streamlines at the angular position of maximum separation (i.e. ϑ=120°) are reported in Fig. 6(a). Different spanwise sections are reported to analyze the flow pattern alterations as one moves towards the blade tip.

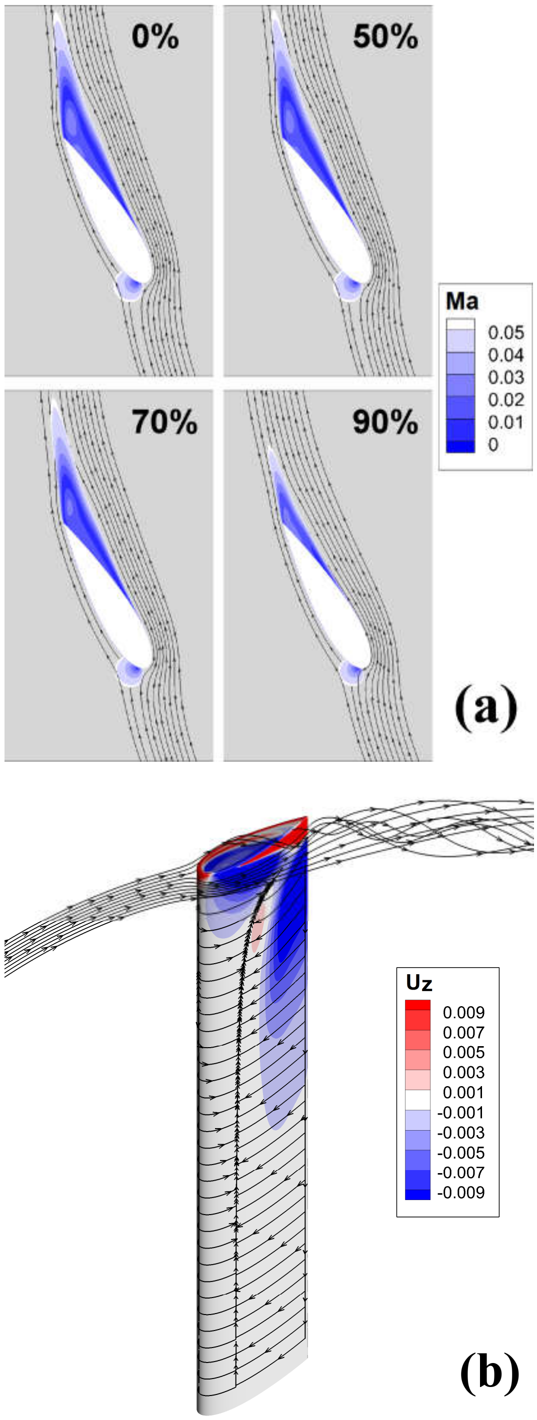

Figure 6 – Downwash effect at ϑ=120°: (a) Mach contours and streamlines at different semispan locations; (b) flow streamlines in the tip region, skin friction lines and z velocity component on the blade surface.

In the central portion of the blade (i.e. from midspan to approximately 70% of the semispan) the flow streamlines lay on a 2D plane and a region of extensively detached flow is present along the entire blade. When moving closer to the tip (90% of the semispan), the discussed effect of the downwash field is apparent: the effective AoA on the airfoil is reduced with respect to that at midspan. As a consequence, the extension of the stall region is also reduced due to the decrease of the incidence angle.

The skin friction lines and contours of the z velocity component on the blade surface reported in Fig. 6(b) show the extension of the region affected by downwash on the suction side of the blade. Near the tip, the flow on the pressure side is no longer able to follow the blade profile, and travels over the tip due to the pressure difference between the pressure side and the suction side. The tip vortex flow is responsible for the downwash velocity component and therefore for the incidence variation along the span, in accordance with the theory of finite wings [48]. It is noted that the finite wing effects occurring in Darrieus rotors are more complex than those encountered in fixed finite wings. This is primarily because of the flow curvature associated with the circular trajectory of the blade, and also the flow nonlinearities due to dynamic stall. To quantify the impact of these effects, relevant outcomes can be obtained by examining the torque coefficient trends per unit length produced by two relevant slices in Fig. 7, e.g. midspan and 80%. The percentage difference between the two curves (i.e. the moment coefficient difference between the curves at each azimuthal angle divided by the average moment coefficient at midspan) is also reported to quantify the dependence of the torque variation on the azimuthal position.

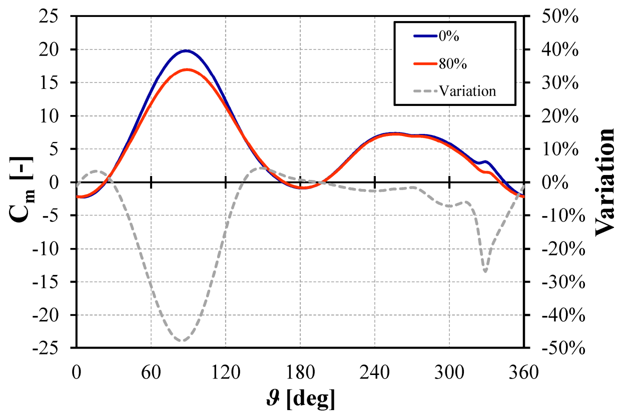

Figure 7 - Comparison of moment coefficient curves at 0% and 80% of the semispan.

It is observed that a notable torque reduction occurs between 40°<ϑ<130°. In addition, large and sudden torque reduction is obtained at the end of the revolution, i.e. when the incidence angle is progressively reducing towards values lower than the stall one. On the other hand, an inversion in the expected trend was noticed close to ϑ=150°, while the torque output is positive. Even if not apparent from the figure, a higher torque production (relative difference of +11% between 80% and midspan) was noticed when getting closer to the tip. According to the finite wing theory, the lift should be in fact always reduced in proximity of the tip and the reduction is assumed to be proportional to the lift itself. Therefore, the inversion at ϑ=150° cannot be justified with this theory only, as well as the significant torque reduction at the end of the revolution, since the reduced load on the blades should not generate such a large downwash effect. Detailed flow analyses will be shown in the continuation of the study to comprehend this phenomenon.

First, the reasons of the sudden torque reduction at the blade tip between 315°<ϑ<340° were investigated. To this purpose, Fig. 8 shows the evolution of the turbulence kinetic energy (TKE) field at selected azimuthal positions based on TKE iso-surfaces. The color scale is based on the intensity of the velocity component along the z-axis (U_z). Three azimuthal positions of the blade are considered in Fig. 8, i.e. ϑ=60° (upper right), 180° (left) and 315° (lower right).

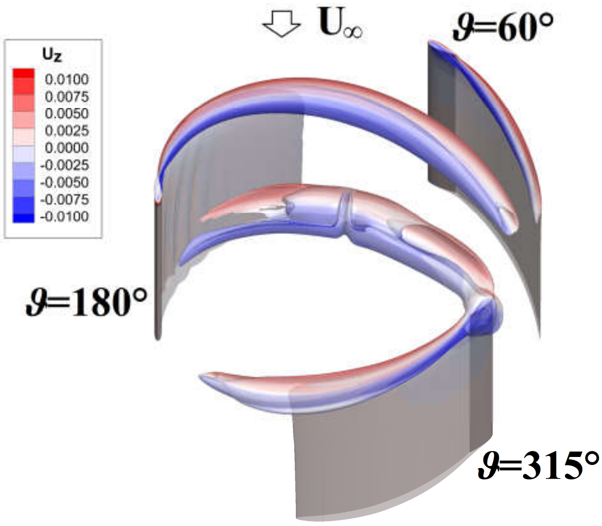

Figure 8 - Iso-surfaces of TKE colored with the contour of U_z.

During the upwind half of the revolution (ϑ=60°) the tip vortex is strong, since the vertical component of velocity is very intense. A high turbulence region is then generated in the tip's wake. For ϑ=180°, U_z is reduced around the blade tip, but the region of the blade wake characterized by high TKE is increased in size and length, and is still associated with large values of U_z. This generates a strong vortex, which is then detached from the blade, after being convected by the wind, is re-encountered by the blade itself at ϑ=315°. The interaction with this macro-vortex induces a more pronounced modification of the torque curve with respect to the 2D case, where this effect is totally absent.

Focusing now on the azimuthal position where the torque inversion takes place, i.e. ϑ=150°, Fig. 9 reports a top view of the flow streamlines at two azimuthal positions. The comparison is carried out with ϑ=48°, which is the other position during the upwind half of the revolution experiencing the same AoA of ϑ=150°. Streamlines on both the pressure and suction sides of the blade are visualized at four different span locations.

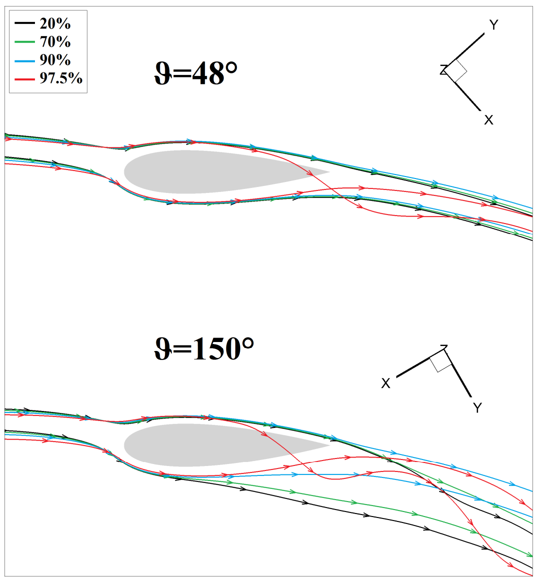

Figure 9 - Streamlines at different span lengths: ϑ=48° and ϑ=150°.

For ϑ=48° the “conventional” downwash effect is clearly visible: moving from midspan to the tip, the incidence of the oncoming flow is progressively reduced and the velocity past the trailing edge is shifted towards the pressure side. This phenomenon is not very pronounced due to the low load on the blade at this angular position and the deflection occurs only in proximity of the tip.

For ϑ=150°, moving from midspan to the tip, the incidence of the oncoming flow is progressively reduced similarly to what is seen at ϑ=48° and no evident difference with respect to the ϑ=48° degrees case can be observed. Conversely, the flow condition on the suction side is completely different: at midspan, even if the AoA is similar to that obtained at ϑ=48°, a large separation region is evident at ϑ=150° due to dynamic stall. As a result of the finite wing effect, a strong modification of the flow is then observed when moving across the blade span towards the tip: starting from 70% semispan, the flow re-starts to be deflected towards the pressure side. At 90% semispan, the flow direction is completely changed with respect to midspan: the separation region is indeed almost absent, making the flow become very similar to that measured at ϑ=48°.

This can be explained by a combined effect of downwash and dynamic stall. During the advancing 90-degree sector of the blade trajectory, only the sections at the tip do not reach stall conditions since they experience a lower AoA. When the incidence decreases in the retreating 90-degree sector, the central portion of the blade suffers from dynamic stall, with a marked reduction of lift production. Conversely, the flow remains attached for the sections at the tip, which are still able to produce the theoretical lift. It can be summarized that, even if the incidence is lower close to the tip, the absence of dynamic stall guarantees higher lift and therefore higher torque production than at midspan in this specific angular position. The explanation is straightforward: when the incidence is maximum, the sections at the tip do not reach stall conditions since they experience lower AoAs and when the incidence decreases they are still able to produce the theoretical lift. It can be summarized that, even if the incidence is lower close to the tip, the absence of dynamic stall guarantees, in this specific condition, higher lift and therefore higher torque production.

Fig. 10 shows an analogous comparison for the angular positions of ϑ=210° and ϑ=300°, which again are characterized approximately by the same AoA value. It can be noticed that the behavior at ϑ=210° is the same of that at ϑ=48°, being an angular position in the downwind half of the rotation where the incidence is increasing (in magnitude). At ϑ=300° the incidence (decreasing) is again the same of ϑ=210° but in this case no evident modification of the streamlines can be observed from midspan to the tip. Indeed, the suction side is characterized by just a slight separation and the downwash effect is very similar to that at ϑ=210°.

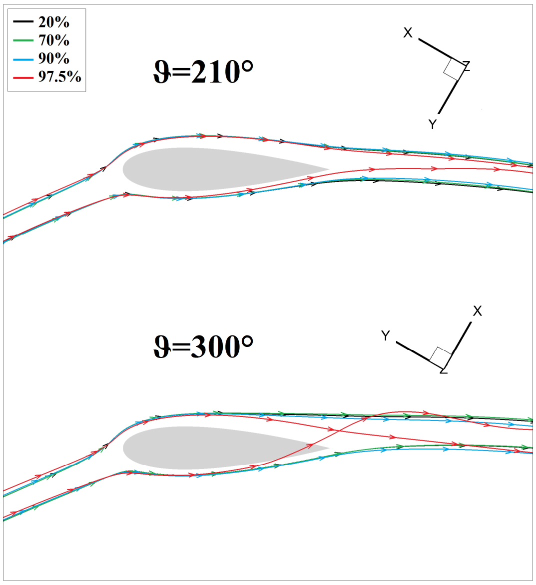

Figure 10 - Streamlines at different span lengths: ϑ=210° and ϑ=300°.

In addition, Fig. 11 shows the streamlines at ϑ=315° to see the effect of the turbulent vortex on the flow field that was described in Fig. 8: it is apparent that a sudden distortion of the incoming flow in the tip region takes place due to the blade-vortex interaction, with a large variation of the incidence angle, which is now not related to the downwash effect.

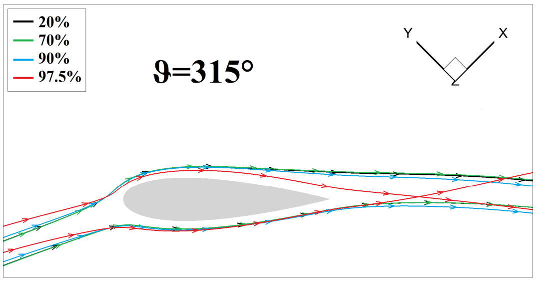

Figure 11 - Streamlines at different span lengths: ϑ=315°.

All aforementioned results can be more quantitatively described by directly evaluating the pressure coefficient (C_p) distributions and the vorticity contours along the blade span.

Fig. 12 reports the pressure coefficient distributions at different span lengths for three of the previously discussed critical angular positions: maximum load (ϑ=80°), inversion of load between midspan and tip (ϑ=150°) and maximum load in the downwind half of the rotation (ϑ=240°). The pressure coefficient used in this study is defined by Eq. (3), where p denotes the static pressure at the airfoil surface. It has to be noted that, due to the complexity of properly defining the actual relative wind speed on the airfoil, the pressure profiles were here normalized by the theoretic relative wind speed (w_{th}) among a null induction factor (i.e. the vectorial sum between the wind speed at infinity U_∞ and the peripheral speed ΩR).

$$C_p = \frac{p - p_\infty}{\frac{1}{2}\rho_\infty w_{th}^2} \tag{3}$$

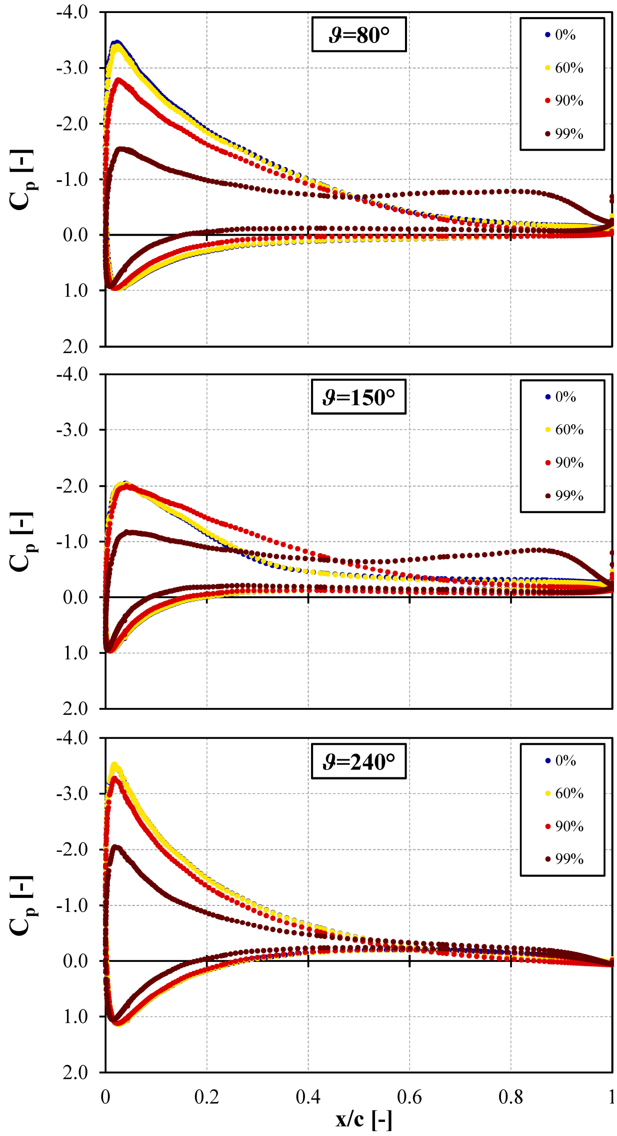

Figure 12 - Pressure coefficient profiles at different span lengths: ϑ=80°, ϑ=150° and ϑ=240°.

In conditions of high load (high AoA and high relative speed, like at ϑ=80°), it is confirmed that the 3D effects can reach up to 40% of the semispan from the tip, since moving from midspan to the tip, the C_p profile at 60% already shows a slight reduction of the load with respect to midspan. Close to the tip, the suction side of the blade is characterized by an almost constant pressure, indicating that this section does generate a very small lift force. As a result, a negative torque production is noticed at this location. When the AoA is high but the relative speed magnitude is lower (ϑ=240°), the 3D effects extend only to the last 20% of the semispan (i.e. from 80% semispan to tip): significant differences in the C_p distribution can be appreciated, however, only above 90% of the semispan. Close to the tip, only a reduction of the load can be observed, without any additional effect. The position ϑ=150° is instead characterized by stalled flow, as shown by the large separation in the pressure distributions at 0% and 60%. In this case, the effect of the tip vortex is to slightly reduce the load, inducing the flow to remain attached to the blade, with a lower separation and even a small improvement of produced lift.

The evolution of the vorticity contours at different span locations along the blade is finally presented in Fig. 13.

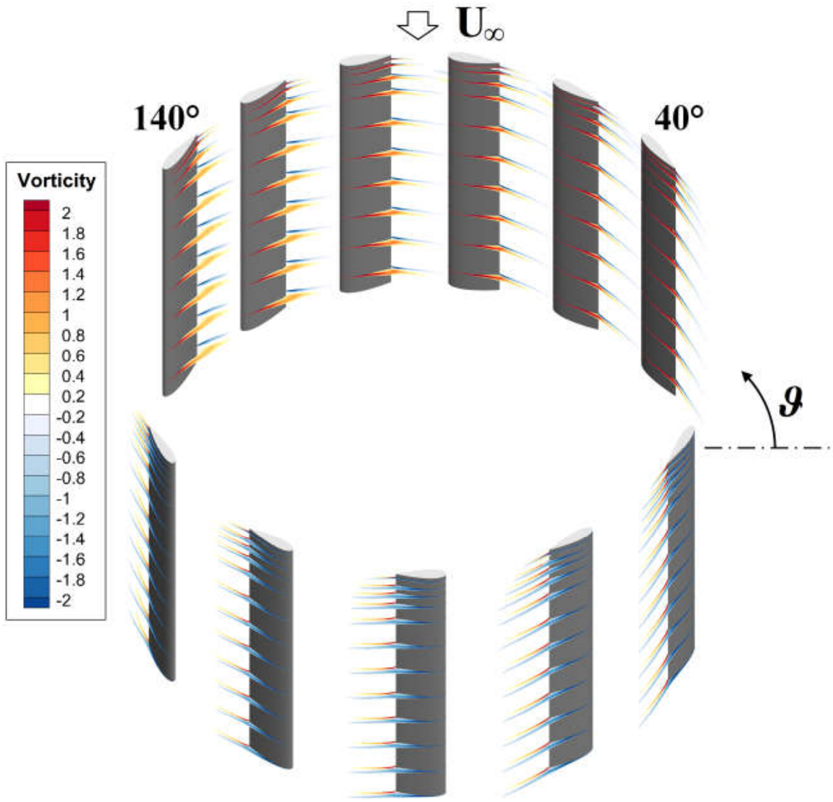

Figure 13 - Vorticity contours at different span lengths during the revolution.

Focusing on the upwind half of the rotation, the two extreme positions of ϑ=40° and ϑ=140°, are in fact of particular interest. It can be noticed that, although (as expected) the behavior in terms of torque distribution along the span is comparable, with analogous values at each span location (see Fig. 3(a) and Fig. 3(b)), the 3D flow field in these two positions is remarkably different. Indeed, for ϑ=40° the vorticity contours are very similar, moving from midspan to the tip, while for ϑ=140° the large separation region due to stall is clearly present along the largest portion of the blade but tends to disappear when getting close to the tip due to tip effects. Moving to the downwind half of the revolution, it is apparent that the vorticity contours are now very similar, moving from midspan to the tip, at all azimuthal positions. This behavior is in agreement with previous analyses of streamlines and pressure coefficient profiles.

5. Concluding remarks

In the study, a 3D, time accurate CFD study of a rotating Darrieus wind turbine blade was carried out. Particular attention was given to the description of 3D flow effects and to the modifications induced by them in comparison to the "infinite-wing" ideal case, which is the one generally optimized by both 2D numerical calculations and low-fidelity simulation models. The main outcomes of the analysis can be summarized as follows:

a) 3D effects do not modify the general trend of torque extraction over the revolution (with the only exception of the near-tip region): indeed, maximum and minimum relative values of torque take place at analogous blade azimuthal positions.

b) The impact of tip effects is strongly dependent on the azimuthal position of the blade, according to oncoming relative speed in terms of incidence angle and modulus. In this view, the accuracy of a low-fidelity model like the BEM theory could be remarkably increased by re-correcting the aerodynamic coefficients for finite-wing effects at each azimuthal position (or streamtube).

c) In the present study case, the average torque reduction due to finite-blade effects corresponded to a reduction of the effective overall blade length of 1.5c (0.75c for each half blade).

d) A strong interaction between the tip-vortex released in the upwind portion of the blade trajectory and the blade moving in the downwind region was noticed in correspondence to an azimuthal position of ϑ=315°.

Future work will include the investigation of 3D flow effects at different tip-speed ratios, particularly the lower ones, at which the impact of dynamic stall is thought to be more relevant, and should also extend the analysis to a three-blade turbine, in order to describe in detail all aspects of wake/blade interactions.

Acknowledgements

We acknowledge use of Hartree Centre resources in this work. The STFC Hartree Centre is a research collaboratory in association with IBM providing High Performance Computing platforms funded by the UK's investment in e-Infrastructure. The Centre aims to develop and demonstrate next generation software, optimised to take advantage of the move towards exa-scale computing. Part of the reported simulations were also performed on two other clusters. One is POLARIS, part of the N8 HPC facilities provided and funded by the N8 consortium and EPSRC (Grant No.EP/K000225/1). The Centre is co-ordinated by the Universities of Leeds and Manchester. The other resource is the HEC cluster of Lancaster University, which is also kindly acknowledged. Finally, thanks are due to Prof. Ennio Antonio Carnevale of the Università degli Studi di Firenze for supporting this research.

References

[1] Paraschivoiu I. Wind turbine design with emphasis on Darrieus concept. Polytechnic International Press: Montreal (Canada), 2002.

[2] Darrieus GJM. Turbine having its rotating shaft transverse to the flow of the current. US Patent No.01835018, 1931.

[3] Tjiu W, Marnoto T, Mat S, Ruslan MH, Sopian K. Darrieus vertical axis wind turbine for power generation I: Assessment of Darrieus VAWT configurations. Renewable Energy 2015; 75(March 2015): 50-67. DOI: 10.1016/j.renene.2014.09.038

[4] Tjiu W, Marnoto T, Mat S, Ruslan MH, Sopian K. Darrieus vertical axis wind turbine for power generation II: Challenges in HAWT and the opportunity of multi-megawatt Darrieus VAWT development. Renewable Energy 2015; 75(March 2015):560-571. DOI: 10.1016/j.renene.2014.10.039

[5] Bianchini A, Ferrara G, Ferrari L. Design guidelines for H-Darrieus wind turbines: Optimization of the annual energy yield. Energy Conversion and Management 2015;89:690-707. DOI: 10.1016/j.enconman.2014.10.038

[6] Balduzzi F, Bianchini A, Carnevale EA, Ferrari L, Magnani S. Feasibility analysis of a Darrieus vertical-axis wind turbine installation in the rooftop of a building. Applied Energy 2012; 97: 921–929. DOI: 10.1016/j.apenergy.2011.12.008

[7] Mohamed MH. Aero-acoustics noise evaluation of H-rotor Darrieus wind turbines. Energy 2014; 65(1): 596-604. DOI: 10.1016/j.energy.2013.11.031.

[8] Bianchini A, Ferrara G, Ferrari L, Magnani S. An improved model for the performance estimation of an H-Darrieus wind turbine in skewed flow. Wind Engineering 2012; 36(6): 667-686. DOI: 10.1260/0309-524X.36.6.667

[9] Mertens S. Wind Energy in the Built Environment. Multi-Science: Brentwood (UK), 2006.

[10] Borg M, Collu M, Brennan FP. Offshore floating vertical axis wind turbines: advantages, disadvantages, and dynamics modelling state of the art. Marine & Offshore Renewable Energy Congress, London (UK), 26-27 September, 2012.

[11] Brahimi M, Allet A, Paraschivoiu I. Aerodynamic analysis models for vertical-axis wind turbines. International Journal of Rotating Machinery 1995; **2**(1): 15-21. DOI: 10.1155/S1023621X95000169

[12] Paraschivoiu I, Delclaux F. Double Multiple Streamtube Model with Recent Improvements. Journal of Energy 1983, 7(3), pp. 250-255.

[13] Bianchini A, Ferrari L, Carnevale EA. A model to account for the Virtual Camber Effect in the Performance Prediction of an H-Darrieus VAWT Using the Momentum Models. Wind Engineering 2011; 35(4): 465-482. DOI: 10.1260/0309-524X.35.4.465

[14] Marten D, Bianchini A, Pechlivanoglou G, Balduzzi F, Nayeri CN, Ferrara G, Paschereit CO, Ferrari L. Effects of airfoil's polar data in the stall region on the estimation of Darrieus wind turbines performance. Proc. of the ASME Turbo Expo 2016, Seoul, South Korea, June 13-17, 2016.

[15] Marten D, Lennie M, Pechlivanoglou G, Nayeri CD, Paschereit CO. Implementation, Optimization and Validation of a Nonlinear Lifting Line Free Vortex Wake Module within the Wind Turbine Simulation Code QBlade. Proc. of the ASME Turbo Expo 2015, Montréal, Canada, June 15-19, 2015.

[16] Deglaire P. Analytical Aerodynamic Simulation Tools for Vertical Axis Wind Turbines. Digital Comprehensive Summaries of Uppsala Dissertations from the Faculty of Science and Technology 2010, 704, ISSN 1651-6214.

[17] Amet E, Maitre T, Pellone C, Achard JL. 2D Numerical Simulations of Blade-Vortex Interaction in a Darrieus Turbine. Journal of Fluids Engineering 2009; 131: 111103.1–111103.15. DOI: 10.1115/1.4000258

[18] Simao-Ferreira C, van Zuijlen A, Bijl H, van Bussel G, van Kuik G. Simulating dynamic stall on a two-dimensional vertical-axis wind turbine: verification and validation with particle image velocimetry data. Wind Energy 2010; 13: 1-17. DOI: 10.1002/we.330

[19] Salvadore F, Bernardini M, Botti M. GPU accelerated flow solver for direct numerical simulation of turbulent flows. Journal of Computational Physics 2013; 235: 129-142. DOI: 10.1016/j.jcp.2012.10.012

[20] Howell R, Qin N, Edwards J, Durrani N. Wind tunnel and numerical study of a small vertical axis wind turbine. Renewable Energy 2010; 35: 412-422. DOI: 10.1016/j.renene.2009.07.025

[21] Raciti Castelli M, Englaro A, Benini E. The Darrieus wind turbine: Proposal for a new performance prediction model based on CFD. Energy 2011; 36: 4919-4934. DOI: 10.1016/j.energy.2011.05.036

[22] Balduzzi F, Bianchini A, Maleci R, Ferrara G, Ferrari L. Critical issues in the CFD simulation of Darrieus wind turbines. Renewable Energy 2016; 85(01): 419-435. DOI: 10.1016/j.renene.2015.06.048

[23] Almohammadi KM, Ingham DB, Ma L, Pourkashan M. Computational fluid dynamics (CFD) mesh independency techniques for a straight blade vertical axis wind turbine. Energy 2013; 58(1 September 2013): 483-493. DOI: 10.1016/j.energy.2013.06.012

[24] Balduzzi F, Bianchini A, Ferrara G, Ferrari L. Dimensionless numbers for the assessment of mesh and timestep requirements in CFD simulations of Darrieus wind turbines. Energy 2016; 97(15 February 2016): 246-261. DOI: 10.1016/j.energy.2015.12.111

[25] Daróczy L, Janiga G, Petrasch K, Webner M, Thévenin D. Comparative analysis of turbulence models for the aerodynamic simulation of H-Darrieus rotors. Energy 2015; 90(1 October 2015): 680-690. DOI: 10.1016/j.energy.2015.07.102

[26] Balduzzi F, Bianchini A, Gigante FA, Ferrara G, Campobasso MS, Ferrari L. Parametric and Comparative Assessment of Navier-Stokes CFD Methodologies for Darrieus Wind Turbine Performance Analysis. Proc. of the ASME Turbo Expo 2015, Montreal, Canada, June 15-19, 2015. DOI: 10.1115/GT2015-42663

[27] Gigante FA, Balduzzi F, Bianchini A, Yan M, Ferrara G, Ferrari L, Campobasso MS. On the Computational Fluid Dynamics Analysis of Darrieus Wind Turbines Using the Reynolds-Averaged Navier-Stokes Equations and the Shear Stress Transport Turbulence Model. Paper submitted for publication to: Energy, 2016.

[28] Bianchini A, Balduzzi F, Ferrara G, Ferrari L. Influence of the blade-spoke connection point on the aerodynamic performance of Darrieus wind turbines. Proc. of the ASME Turbo Expo 2016, June 13-17, Seoul (South Korea), 2016.

[29] Lam HF, Peng HY. Study of wake characteristics of a vertical axis wind turbine by two- and three-dimensional computational fluid dynamics simulations. Renewable Energy 2016; 90(May 2016): 386-398. DOI: 10.1016/j.renene.2016.01.011

[30] Ghosh A, Biswas A, Sharma KK, Gupta R. Computational analysis of flow physics of a combined three bladed Darrieus Savonius wind rotor. Journal of the Energy Institute 2015; 88(4): 425-437. DOI: 10.1016/j.joei.2014.11.001

[31] Raciti Castelli M, Pavesi G, Battisti L, Benini E, Ardizzon G. Modeling strategy and numerical validation for a Darrieus vertical axis micro-wind turbine. Proc. of the ASME 2010 International Mechanical Engineering Congress & Exposition (IMECE), Vancouver, British Columbia, Canada, November 12-18, 2010. DOI: 10.1115/IMECE2010-39548

[32] Untaroiu A, Wood HG, Allaire PE, Ribando RJ. Investigation of Self-Starting Capability of Vertical Axis Wind Turbines Using a Computational Fluid Dynamics Approach. ASME Journal of Solar Energy Engineering 2011; 133(November 2011): 041010-1-8. DOI: 10.1115/1.4004705

[33] Gosselin R, Dumas G, Boudreau M. Parametric study of H-Darrieus vertical-axis turbines using uRANS simulations. Proc. of the 21st Annual Conference of the CFD Society of Canada, May 6-9, Sherbrooke (Canada), 2013

[34] Alaimo A, Esposito A, Messineo A, Orlando C, Tumino D. 3D CFD Analysis of a Vertical Axis Wind Turbine. Energies 2015; 8: 3013-3033. DOI: 10.3390/en8043013

[35] De Marco A, Coiro DP, Cucco D, Nicolosi F. A Numerical Study on a Vertical-Axis Wind Turbine with Inclined Arms. International Journal of Aerospace Engineering 2014; 2014: 1-14. DOI: 10.1155/2014/180498

[36] Raciti Castelli M, Benini E. Effect of Blade Inclination Angle on a Darrieus Wind Turbine. ASME Journal of Turbomachinery 2012; 134(May 2012): 031016-1-10. DOI: 10.1115/1.4003212

[37] Orlandi A, Collu M, Zanforlin S, Shires A. 3D URANS analysis of a vertical axis wind turbine in skewed flows. Journal of Wind Engineering and Industrial Aerodynamics 2015; 147(December 2015): 77-84. DOI: 10.1016/j.jweia.2015.09.010

[38] Bedon G, De Betta S, Benini E. A computational assessment of the aerodynamic performance of a tilted Darrieus wind turbine. Journal of Wind Engineering and Industrial Aerodynamics 2015; 145(October 2015): 263-269. DOI: 10.1016/j.jweia.2015.07.005

[39] Dossena V, Persico G, Paradiso B, Battisti L, Dell'Anna S, Brighenti A, Benini E. An Experimental Study of the Aerodynamics and Performance of a Vertical Axis Wind Turbine in a Confined and Non-Confined Environment. Proc. of the ASME Turbo Expo 2015, Montreal, Canada, June 15-19, 2015

[40] Rainbird J, Bianchini A, Balduzzi F, Peiro J, Graham JMR, Ferrara G, Ferrari L. On the Influence of Virtual Camber Effect on Airfoil Polars for Use in Simulations of Darrieus Wind Turbines. Energy Conversion and Management 2015;106:373-384. DOI: 10.1016/j.enconman.2015.09.053

[41] Campobasso MS, Piskopakis A, Drofelnik J, Jackson A. Turbulent Navier-Stokes Analysis of an Oscillating Wing in a Power Extraction Regime Using the Shear Stress Transport Turbulence Model. Computers and Fluids 2013; 88: 136-155. DOI: 10.1016/j.compfluid.2013.08.016

[42] Drofelnik J and Campobasso MS, Comparative Turbulent Three-Dimensional Navier-Stokes Hydrodynamic Analysis and Performance Assessment of Oscillating Wings for Renewable Energy Applications, International Journal of Marine Energy, Vol. 16, 2016, pp. 100-115

[43] Campobasso MS, Gigante F, Drofelnik J. Turbulent Unsteady Flow Analysis of Horizontal Axis Wind Turbine Airfoil Aerodynamics Based on the Harmonic Balance Reynolds-Averaged Navier-Stokes Equations. ASME paper GT2014-25559, Proc. of the ASME Turbo Expo 2014, Düsseldorf (Germany), 2014. DOI:10.1115/GT2014-25559.

[44] Campobasso MS, Drofelnik J, Gigante F, Comparative Assessment of the Harmonic Balance Navier-Stokes Technology for Horizontal and Vertical Axis Wind Turbine Aerodynamics, Computers and Fluids, Vol. 136, 2016, pp. 354-370.

[45] Campobasso MS, Baba-Ahmadi MH. Analysis of Unsteady Flows Past Horizontal Axis Wind Turbine Airfoils Based on Harmonic Balance Compressible Navier-Stokes Equations with Low-Speed Preconditioning. ASME Journal of Turbomachinery 2012; 134(6): 061020-1-13. DOI: 10.1115/1.4006293.

[46] Menter FR. Two-equation Turbulence-models for Engineering Applications. AIAA Journal 1994; 32(8): 1598-1605. DOI: 10.2514/3.12149

[47] http://community.hartree.stfc.ac.uk/wiki/site/admin/resources.html, last accessed 10/05/2016.

[48] Abbott IH, Von Doenhoff AE. Theory of Wing Sections. New York, USA: Dover Publications Inc.; 1959.